PHYSICAL REVIEW E **69**, 026307 (2004)

Experimental study of surface waves scattering by a single vortex and a vortex dipole

Francisco Vivanco and Francisco Melo
Departamento de Física de la Universidad de Santiago de Chile and Centro para la Investigación Interdisciplinaria Avanzada en Ciencia de los Materiales, CIMAT, Avenida Ecuador 3493, Casilla 307, Correo 2, Santiago, Chile

(Received 18 July 2003; published 27 February 2004)

Surface waves interacting with filamentary vortex offer an interesting tool to characterize static and dynamics of surface vorticity. An experimental study of the scattered wave by a single vortex as well as by a vortex dipole is reported. On a plane wave front, the vortex circulation introduces a spatial phase shift that gives rise to dislocated waves. Dislocations can be explained by the effect of the differential advection due to the vortex flow, on the propagating wave front. Both the Burgers vector of dislocations and the scattering cross section are measured in the deep water regime. The analogy between the wave-vortex interaction and the Aharonov-Bohm effect in quantum mechanics is explored by contrasting the Burgers vectors of dislocations as well as the form of the scattered wave in both cases. For the case of the hard core vortex, spiral waves are observed in agreement with theoretical works on both the Aharanov-Bohm effect and classical surface wave mechanics.

DOI: 10.1103/PhysRevE.69.026307 PACS number(s): 47.32.Cc, 47.35.+i, 67.40.Vs

I. INTRODUCTION

It is well accepted that coherent structures such as vortex filaments are prominent features of turbulent flows [1]. Also, vortex stretching is believed to be a major ingredient in the cascade of energy from large to small scales, which is characteristic of those flows. However, due to the technical difficulties of nonintrusive experimental methods, the characterization of vortical structures is still poor. Recently, it has become apparent that it is possible to obtain valuable information about vorticity fields by looking at their interaction with a mechanical wave. For instance, Baudet and coworkers [2] have characterized a von Kármán array of vortices and studied the effect of vorticity on a plane fronted ultrasonic wave. Although in this case the analysis of the scattered wave allows us to deduce the frequency shift introduced by the advection of the vorticity field, a detailed description of the scattered wave is well beyond the current experimental capabilities. Studies carried out by Roux and Fink [3,4] with a single vortex have obtained in the acoustical case, by using time-reversal techniques, valuable information about vortex size and vortex circulation. Further improvements of these techniques have been achieved by Manneville and co-workers [5,6]. For instance, by using the double time-reversal mirrors these authors have obtained a complete characterization of the vortex dynamics, such as the temporal evolution of its size, its circulation, and its position. For a turbulent vortex in air, Labbé and Pinton [7] have used an adaptative-coherent average technique to reconstruct the amplitude and the phase of the distorted acoustical front wave near the vortex core. As in all the cases described above, these results have been obtained when wavelength of the acoustical wave is small compared to the vortex core size.

However, to our knowledge, for all the acoustical methods used at present, a full visualization of the scattered wave is still an unresolved issue. In order to overcome part of these difficulties, we have undertaken a study of the interaction of surface waves with surface vorticity in deep water. This problem is also of interest in its own right in order to characterize surface flows in rivers, lakes, and seas [8,9]. An important fact is that the interaction of vorticity with surface waves is quite analogous to its interaction with acoustic waves, and thus it provides additional insight into the general problem of vortex wave interaction. Also, as pointed out in a remarkable work of Berry *et al.* [10], this problem presents a classical mechanical analog of the Aharonov-Bohm effect in quantum mechanics [11]. Exploring this analogy further, both analytically and experimentally [12,13], we have shown that there are indeed similarities as well as differences with the Aharonov-Bohm effect; among the former, a dislocation in the wave front that is proportional to the vortex circulation, and among the latter, a significant change in the symmetry of the scattered wave. This difference is due to the fact that, as opposed to quantum mechanics in whose work frame electrons can not penetrate the solenoid, a surface wave does penetrate inside the vortex when the water surface deflection induced by the fluid rotation is small.

Here we report on an experimental study in the deep water regime of the scattering of surface water waves by both, a single vortex and a vortex dipole. In this paper we describe in detail the experimental aspects of the surface wave problem. Our presentation is organized in seven sections as follows. In Sec. II, we introduce most of the experimental considerations, such as surface wave visualization, water level control, as well as vorticity generation and its control. Section III is devoted to surface wave characterization. We describe the experimental techniques used to measure phase and amplitude of surface waves. Measurements of the dispersion relation, phase, and group velocities of the waves are presented as well. In Sec. IV, our method to measure the surface velocity field is described. Additionally, we characterize surface deflections at the vortex core, we link these measurements to the vorticity field, and we apply the meniscus method to measure water surface tension. Section V is divided into six subsections in which we present complementary results to our previous investigations [12,13]. In Secs. V A and V B we present measurements of the phase shift induced on the incident wave by the interaction with a vorticity field as well as a simple interpretation of these re-

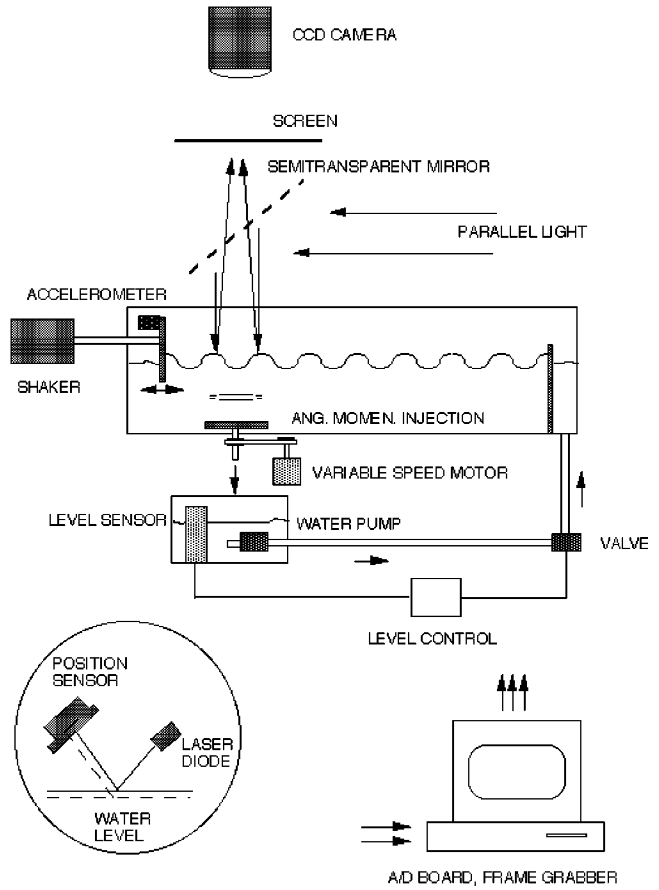

FIG. 1. Sketch of experimental setup for surface wave visualization. Inset, schema of the level detector for the level control of the water tank.

sults, based on the wave advection. In Sec. V C, our measurements of the scattered wave amplitude are contrasted to theoretical findings. In particular, in Sec. V D, for the case of a hard core vortex, we show experimentally that the scattered surface wave is spiral shaped. In Sec. V E, by performing an explicit calculation of the scattered wave, based on the theoretical work of Coste *et al.* [14], in the shallow water regime, we obtain the existence conditions for such spiral waves. The same type of calculations, based on the work of Berry *et al.* [10], show that the scattered wave describing electrons is spiral shaped as well.

Section VI is devoted to the qualitative study of a vortex dipole configuration. Finally, a brief discussion is given in the final remark section. Theoretical work is not included since it has been well documented in Refs. [14–16]. However, experimental findings are contrasted to the available theoretical results.

II. EXPERIMENTAL SETUP

In our experiment, a planar wave front is excited by moving horizontally a rigid dipper at the surface of a water tank, as presented in Fig. 1, at frequencies and amplitudes that range from 5 to 40 Hz and from 0.1 to 1 cm, respectively. Water tank is 150 cm long, 80 cm wide, and 40 cm height. In order to visualize the scattered wave, the free surface of the fluid was illuminated from above with a parallel beam. A semitransparent mirror located at 45° with respect to the horizontal deviates a horizontal incident beam providing homogeneous and perpendicular lighting. The light reflected on the wavy surface of water crosses the mirror and forms caustic lines on a horizontal screen located 50 cm above the surface water. The patterns on the screen are registered by a video camera and stored into a computer by a frame grabber.

The vortex forms spontaneously when letting the water come out of the tank, at rate $Q\sim 10\ \mathrm{cm}^3/\mathrm{s}$ through a hole of 6 mm in diameter at the bottom of the tank. The vortex circulation can be enhanced by rotating, at rate f_d lower than 1.5 Hz, around its principal axis a disk of 15 cm diameter and located close to the bottom of the tank. The disk axis coincides both with the center of the hole and the vortex core so that the injected angular momentum adds to the vorticity field. The distance from the water level to the disk is about 10 cm. Thus, the rotating disk does not affect the boundary conditions for the surface waves whose penetration length is less than 5 mm for our experimental conditions. It is essential to keep the water level constant and free of external vibration to obtain good stability as well as repeatability of the experimental results. This is achieved by pumping the outflowing water back into the tank. A porous wall, separating the observation region from the water injection one, avoids surface fluctuations due to water flow. In addition, an automatic feedback system was designed to control the water level to better than 2×10^{-2} mm. It is composed of a level sensor, a conventional proportional-integro-differential (PID) system, and a needle valve adjusted by a stepping motor. As a level detector, we have used a linear photodiode sensor and a laser diode as shown in the left inset of Fig. 1. This detector is mounted on a disk that is the upper lid of the porous vertical cylinder, acting as a filter for rapid fluctuations of the water level, and indicated as level sensor in the setup sketch.

III. VORTEX CHARACTERIZATION

Vorticity is characterized by two methods depending on vortex circulation. For the case of small circulation, we have developed a particle tracking method which consists of following with a video camera small particles located on the free surface of water. In order to increase contrast of the video images, particles were illuminated using white grazing light. For low rotation rates our results show that the vortex azimuthal velocity decreases as $1/r$; see Fig. 2.

Additionally, our particle tracking measurements show that radial fluid speed at water surface is about 2% of the tangential one. Vortex circulation, $\Gamma=\oint\vec{U}(\vec{r})\cdot d\vec{r}$, is then approximately constant except within the vortex core.

When vortex circulation is increased, surface deflections due to fluid rotation become visible. From lateral pictures of such deflections and by using border detection we obtain the surface deformation profile (see Fig. 3). This can be fitted to a Lorentzian except close to the vortex core where the fit is parabolic. In our case, the tangential fluid speed can be calculated directly from the relation

$$U^2(r)/2+gz-\sigma C=0, \tag{1}$$

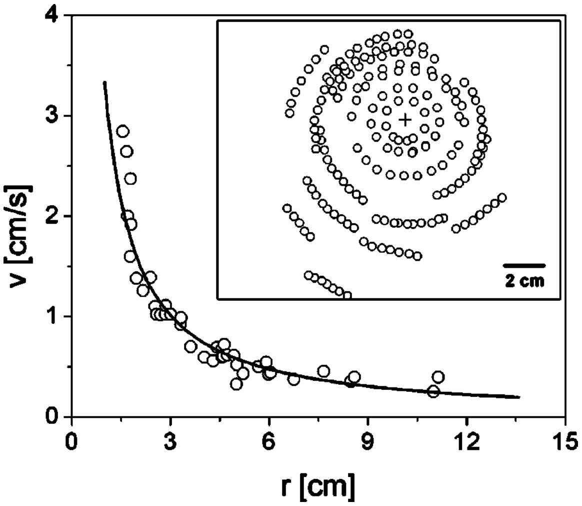

FIG. 2. Typical vortex azimuthal velocity, in water of 10 cm depth, surface tension $\sigma \approx 63$ erg/cm^2, and disk rotation frequency $f_d = 0.13$ Hz, obtained by the particle tracking method. Solid line is the $1/r$ fit to the data. Inset: Typical particle trajectories around the vortex core.

which traces back pressure equilibrium at the free surface [17]. Here $U(r)$ is the tangential fluid speed, r and z are the radial and vertical coordinates, respectively (with origins in the vortex core), σ is the water surface tension, g is the acceleration of gravity, and C is the curvature of the free surface. From surface deflection measurements and the relation (1), we found that the fluid at the vortex core rotates as a rigid body, i.e., with constant angular speed, whereas the tangential velocity far from the vortex core decays approximately as $1/r$, in agreement with the results obtained by the particle tracking method. The vortex core size is defined by the crossover where tangential velocity changes from $1/r$ to r dependence. The vortex diameter is about 4 mm at low circulation. However, for large circulations, surface deflections due to the fluid rotation become important affecting the propagation of surface wave through the vortex. Thus, for large Γ (>30 cm^2/s), at the penetration scale of the flow associated with surface waves (of the order of $\lambda/3$), the vortex core is seen as an air core into which waves no longer penetrate. According to our estimate of the vortex core size, our experiments belong to the case in which the wave vector of the incident wave times the vortex core size, ka, is slightly larger than one.

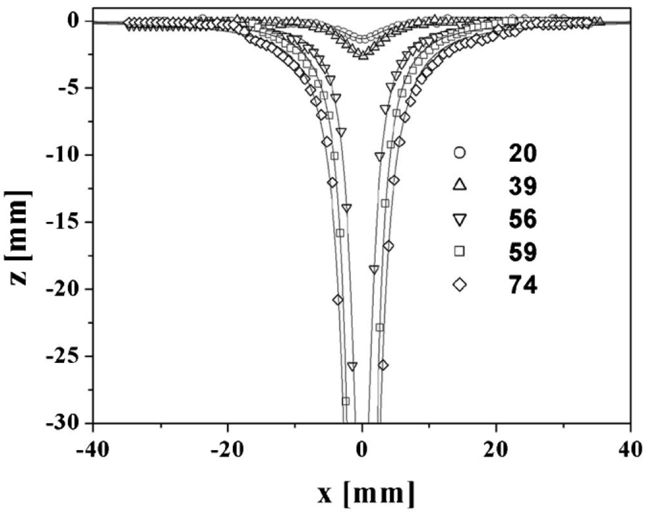

FIG. 3. Side view of surface deflection induced by different values of vortex circulation Γ in cm^2/s.

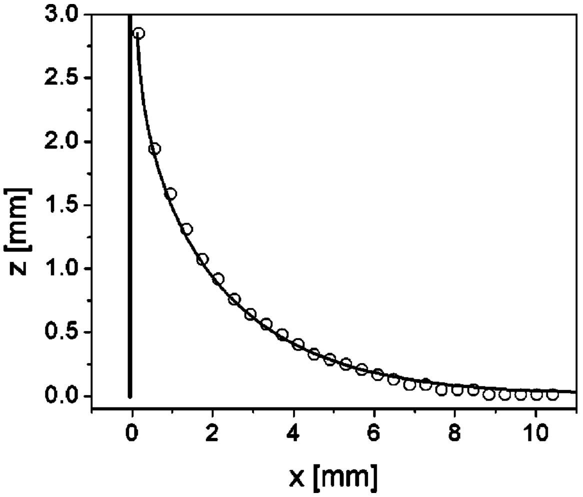

FIG. 4. Experimental meniscus profile. The solid line is the fit obtained by adjusting κ in the theoretical expression for the meniscus. The vertical line represents the surface of a glass plate used to form the meniscus.

Our experiment is sensitive to surface tension of water. In order to measure σ, we study the meniscus formed when the water-air interface reaches a vertical wall. The meniscus is formed on a vertical glass plate, previously cleaned to avoid hysteresis on the contact angle. It is well known [20] that in this case, the meniscus profile is given by

$$\kappa x = \operatorname{arc\,cosh}\left[\frac{2}{\kappa z}\right] + 2\left[1-\left(\frac{\kappa z}{2}\right)^2\right]^{1/2} - \operatorname{arc\,cosh}\left[\frac{1}{\sin\left(\frac{\pi}{4}-\frac{\alpha}{2}\right)}\right] - 2\cos\left(\frac{\pi}{4}-\frac{\alpha}{2}\right), \qquad (2)$$

where $\kappa = (\rho g/\sigma)^{1/2}$ is the capillary length, α is the contact angle, and x and z are the horizontal and vertical coordinates, respectively, as denoted in Fig. 4. In addition, the location of the contact line in the z direction, z_{max}, is given by $\kappa z_{max} = 2\sin(\pi/4 - \alpha/2)$. Figure 4 is the experimental meniscus profile obtained from digital images using border detection. Surface tension is obtained by adjusting κ in the theoretical shape for the meniscus. For several measurements in time, we observe that σ decreases until it nearly stabilizes at $\sigma \approx 63$ erg/cm^2. This decrease in σ is a well-known effect and it is due to the presence of impurities on the surface of the water. With this method the error in determining σ is less than 5% and is mainly due to inaccuracy of the contact angle measurements. To avoid variations of surface tension water is removed periodically from the tank. In addition, as ex-

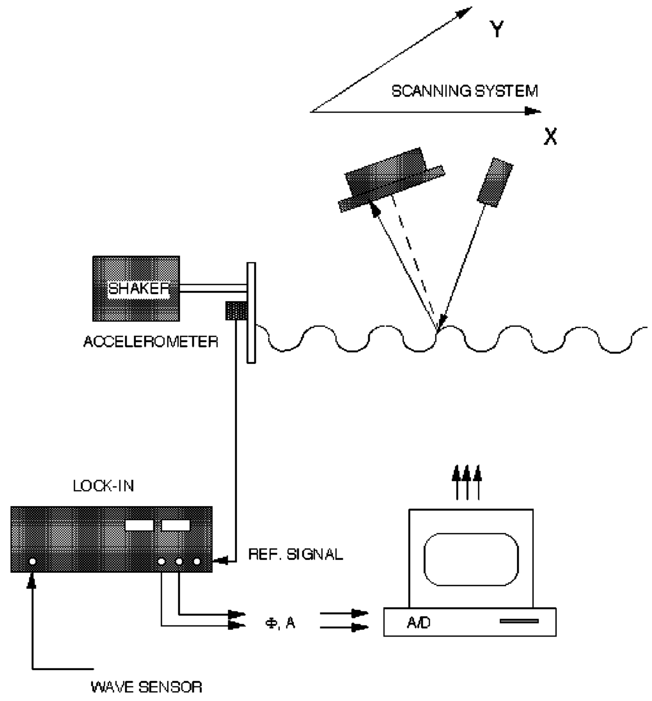

FIG. 5. Schema of the experimental setup for the measurements of the phase and the amplitude of surface waves.

plained below, we check the value of surface tension during the experiment by measuring the dispersion relation of the surface waves. The experiments reported below have been performed for the indicated value of $\sigma \approx 63$ erg/cm^2.

IV. SURFACE WAVE CHARACTERIZATION

In order to determine accurately the phase and the amplitude of the wave, we have developed an experimental method in which both quantities are measured at several locations around the vortex. Our method consists in measuring the deflection of a laser beam that is reflected at the wavy free surface of the fluid (quantitative information about wave amplitude is not available from low resolution images). Laser deflection is detected by a two-axis position sensor. A homemade *x*-*y* displacement system, computer controlled, located just above the fluid provides the horizontal motion to scan the whole surface (see Fig. 5). A lock-in amplifier is used to measure the phase and the amplitude of the scattered wave, with respect to the incident wave, and to filter the noise due to external vibrations. As discussed by Douady [18], the local slope at the water surface is directly related to the laser deflection.

Experimental parameters, such as frequency and amplitude of the excitation signal that control the deeper movement, the rotation rates of the disk, and the location of the sensor of both the wave phase and the wave amplitude, are set and checked periodically by a PC computer. To determine the wavelength λ, we have measured the relative phase of the wave Φ (referred to the excitation signal), along a line parallel to the wave vector for several values of the excitation frequency. As expected for surface waves, Φ varies linearly with the distance from the source, *x*. This is shown in Fig. 6. Then, it is straightforward to obtain the wavelength by identifying the slopes of the straight lines, Φ vs *x*, as $2\pi/\lambda$. From these measurements the dispersion relation for surface waves was directly obtained, see Fig. 7. The solid line in this figure corresponds to the theoretical dispersion relation in the deep water regime [19],

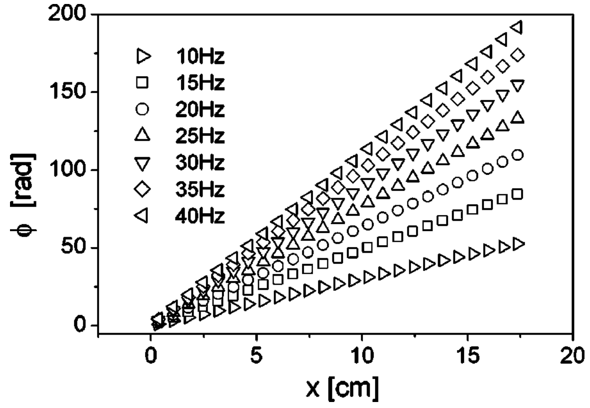

FIG. 6. Φ as a function of distance, *x*, for several values of *f*. Slope of the straight lines is $2\pi/\lambda$.

$$\omega^2 = gk + \sigma k^3/\rho \tag{3}$$

in which we have used σ as an adjustable parameter. The value of σ obtained in this manner is close to that obtained by the meniscus measurements discussed previously. However, the fit of σ in the relation dispersion is more accurate than the meniscus method, giving errors less than 2%. On the other hand, group velocity V_g can be obtained by measuring Φ as a function of ω at a given distance L from the source. The local slope of this curve [see Fig. 8(a)] relates to V_g as

$$V_g = L\,d\omega/d\Phi. \tag{4}$$

Figure 8(b) presents the group velocity V_g and phase velocity V_ϕ as a function of frequency. (V_ϕ is calculated directly from the experimental relation dispersion as $V_\phi = \omega/k$.) Since we are interested in measuring the scattering of a wave by a vortex, wave attenuation as a function of distance becomes a relevant issue. It is well known that because of

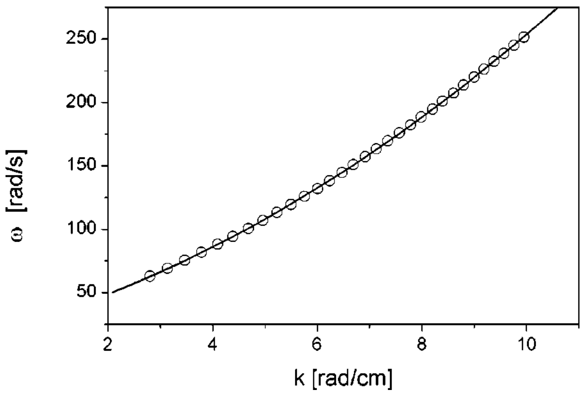

FIG. 7. Relation dispersion of surface waves. The solid line is the best fit obtained from the theoretical relation dispersion, Eq. (3), using σ as a fitting parameter.

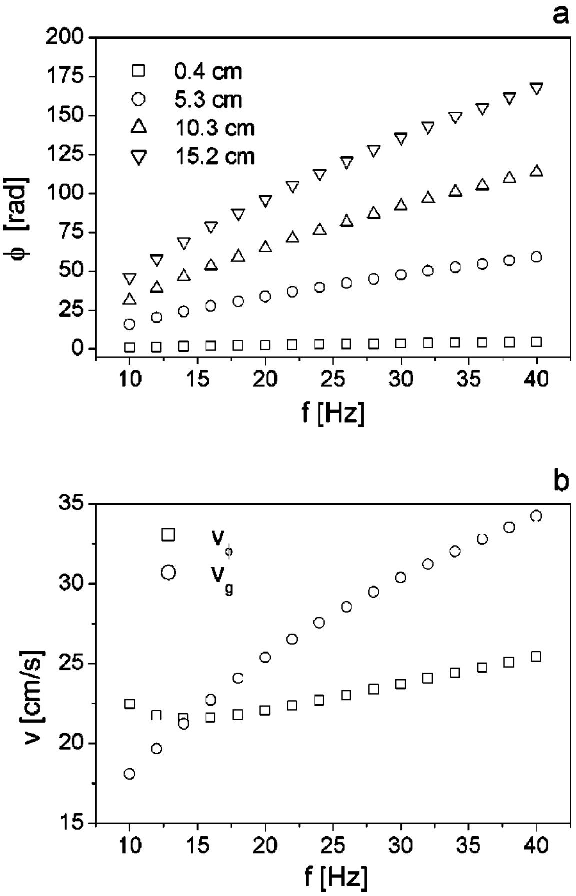

FIG. 8. (a) Φ as a function of f for several distances from the source. (b) Group velocity V_g and phase velocity V_ϕ of waves as a function of f.

viscous damping the amplitude of the wave decreases like $\exp(-x/l_\nu)$, where x is the distance from the source. The attenuation characteristic distance l_ν was measured as a function of frequency, and results were plotted in Fig. 9. As expected from a viscous attenuation in the capillarity wave regime, l_ν decreases approximatively as $1/f$ [19].

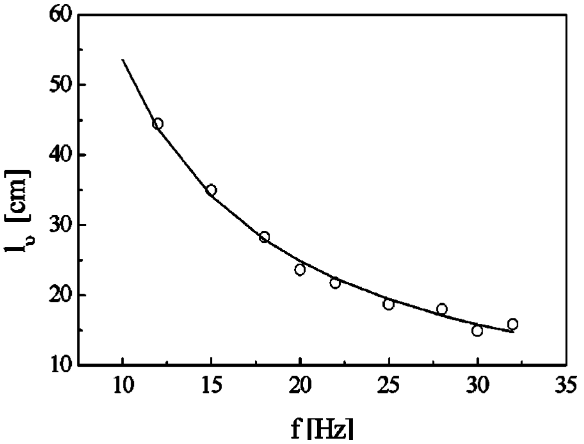

FIG. 9. Characteristic damping length l_ν as a function of f. The solid line corresponds to $1/f$ which is the scaling obtained theoretically for a surface wave in the low dissipative regime.

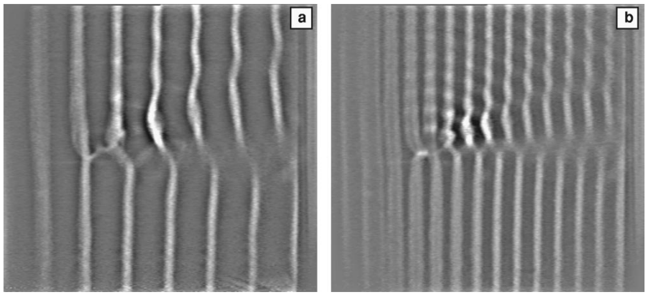

FIG. 10. Surface visualization for $\Gamma \sim 12$ cm^2/s; (a) $f=9$ Hz, wavelength $\lambda = 2.4$ cm, and $V_g = 15.5$ cm/s; (b) $f=17$ Hz, $\lambda = 1.16$ cm, and $V_g = 20.5$ cm/s.

V. SURFACE WAVE-VORTEX INTERACTION

A. Wave front dislocations

Figure 10 shows interference patterns produced by surface waves interacting with a vortex for two different frequencies at constant vortex circulation. In both figures, the incident wave propagates from left to right and the vortex is counterclockwise. It is observed that following a line parallel to the incident wave vector and containing the vortex core, the wave front has a discontinuity which corresponds to a jump in the phase of the wave. Due to the fluid motion, in the upper side of the figures the wave is dilated with respect to the incident one, whereas the wave in the lower part is compressed. The global effect of the advection is to produce phase discontinuities in the wave front. As pointed out by Berry *et al.* [10], such discontinuities are similar to the ones that occur in the wave function in the Aharanov-Bohm effect. Although discontinuities of this type constitute the analog of dislocations of an atomic plane in a crystal, they represent a more general class of dislocations for which fractionary values of Burgers vector are allowed. Here, the Burgers vector is defined through $b/\lambda = \Delta\phi/2\pi$ and represents the change in the phase of the incident wave. More analogies of our surface waves' experiment with the Aharonov-Bohm effect are discussed further in the text. The wave patterns at constant frequency for several values of Γ are shown in Fig. 11. For small Γ, see Fig. 11(a), the wave front exhibits a continuous phase change when going from the lower to the upper region of the figure. The scattered wave, which is visible only in the upper part of the figure, propagates following an axis which makes a small angle with respect to the incident wave vector. In Fig. 11(b) the scattered wave is still visible only in the upper region but the phase shift has increased, giving rise to a discontinuity similar to the one in Fig. 10(b). In contrast, Fig. 11(c) shows a clear difference with respect to previous ones: the wave front is continuous but it exhibits an additional wavelength in the upper region; the Burgers vector is in this case equal to 1. The scattered wave, still located in the upper region, propagates mainly perpendicular to the incident direction. Finally, for a Burgers vector $b = 1.5\lambda$, as in Fig. 11(d), the scattered wave becomes also visible in the lower region.

We have quantified the Burgers vector by measuring the relative phase of the dislocated wave with respect to the incident plane wave. The phase shift of the dislocated wave

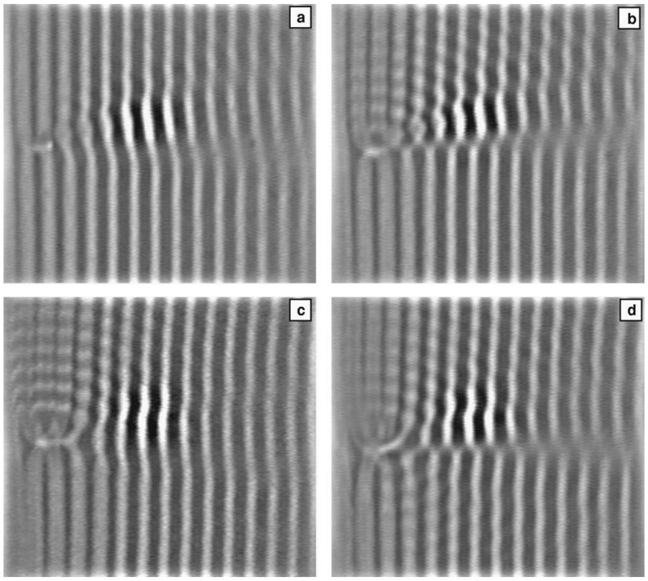

FIG. 11. (a) Experimental surface visualization for constant frequency $f=20$ Hz, $\lambda=1.0$ cm, $V_g=22.2$ cm/s, and varying Γ; (a) $\Gamma\sim4$ cm^2/s, (b) $\Gamma\sim11$ cm^2/s (c) $\Gamma\sim21$ cm^2/s and (d) $\Gamma\sim33$ cm^2/s.

front, measured along a line parallel to the incident nondeformed wave front and located 10 cm away from the vortex, is presented in Fig. 12(a) for several frequencies and for a constant circulation Γ. It is observed that the phase shift has a jump when crossing the dislocation line. Measurements of such a jump phase $\Delta\phi$ give directly the fractional part of the Burgers vector b, associated with wave front dislocations since $\Delta\phi/2\pi=b/\lambda$.

In Fig. 12(b) we present the product of Burgers vector and the group velocity V_g for several values of the circulation Γ. Experimental results show that this product is nearly independent of frequency but increases with Γ. We have also checked that Burgers vector is a linearly increasing function of Γ. Figure 13 illustrates this result, which is obtained by taking the frequency average of the data presented in Fig. 12(b). In summary, the Burgers vector is, in agreement with theoretical calculations for the nearly deep water regime [14], not only a function of f or λ but also a linear function of Γ, satisfying the relation $b/\lambda\approx\Gamma/V_g\lambda$. An analogous linear relation is also predicted by the Berry calculation for the phase shift introduced by the vector potential in the wave function of quantum electrons. This is discussed in more detail in following sections.

B. Wave advection

In this section, we show in a simple manner that the existence of dislocations in the wave front is a result of both a compression and a dilation of the wave, induced by the vortex flow when the wave crosses the vorticity region. Without loss of generality, let us first consider a region in which a surface wave propagates along the direction of the speed gradient, x. Then, the frequency in the laboratory frame reads

$$\omega(x)=\omega_V(x)+kV(x), \tag{5}$$

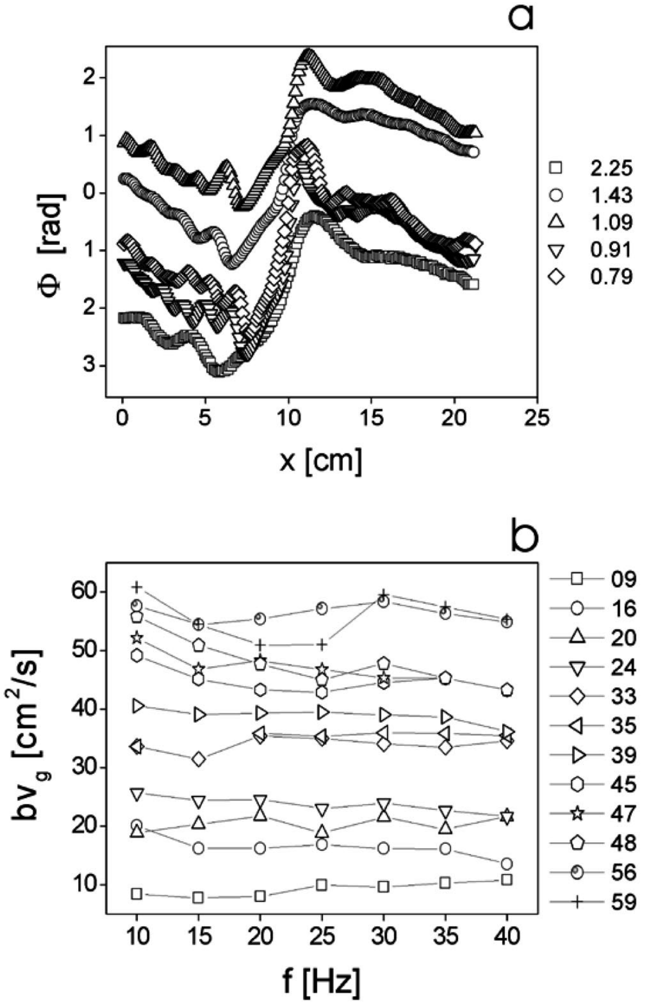

FIG. 12. (a) Phase shift of the dislocated wave for several wavelengths λ and a constant circulation $\Gamma\sim14$ cm^2/s. In the figure λ are in centimeters. Phase shift is measured along a line parallel to the incident wave front and located at a distance (measured along the propagation direction) of 10 cm ahead the vortex core. (b) The product bV_g as a function of f for several values of Γ. The units of Γ are cm^2/s.

where $V(x)$ is the fluid velocity and k is the wave vector which is linked to ω_V through the dispersion relation of surface waves in deep water. Since the phase of the wave is conserved $\omega(x)$ must be a constant, independent of the coordinate x. This constraint relies on the fact that there are neither sources nor sinks of front waves within the region of interest. Differentiating the former relation, we obtain the wave vector variation in space,

$$\frac{dk}{dx}=-k\frac{dV/dx}{V_g+V}, \tag{6}$$

where V_g is the surface wave group velocity. Thus the wave front is dilated if the gradient of speed is positive whereas it is compressed in the opposite case. In the case of $V_g\gg V$, which is not always satisfied in our system, the total variation of the local k with respect to the incident wave vector k_0 at a given position $x>0$ reads

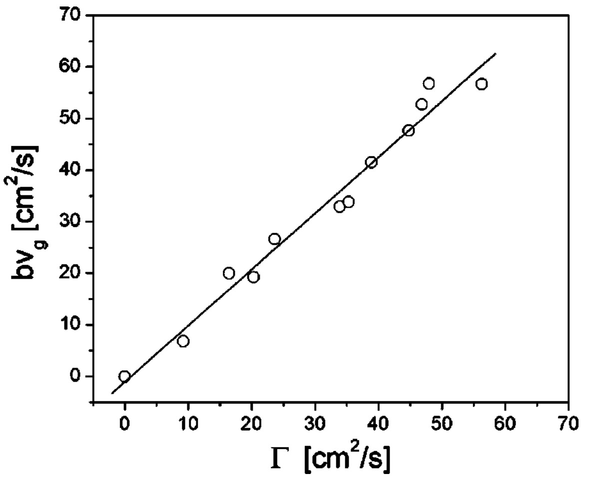

FIG. 13. The Burgers vector of dislocations times the group velocity, bV_g, as a function of Γ.

$$\Delta k=\int_0^x \frac{dk}{dx'}dx' \sim -k_0\frac{V(x)}{V_g}. \tag{7}$$

Here, without losing generality, we have assumed that $V=0$ and $dV/dx=0$ for $x<0$. The total variation of the wave phase, $\Delta\phi_x$, with respect to the incident wave front, at the position x, is therefore

$$\Delta\phi_x=-\int_0^x k_0\frac{V(x')}{V_g}dx'. \tag{8}$$

For the case of a vortex, the total phase shift of the wave in a circuit including the vortex core is

$$\Delta\phi_x/2\pi=\frac{b}{\lambda}=\frac{1}{V_g\lambda}\oint \vec{V}(\vec{x})\cdot d\vec{x}=\frac{\Gamma}{V_g\lambda}, \tag{9}$$

which is the formula deduced rigorously by Coste *et al.* [14] as a first approximation to the deep water regime for low Mach numbers, $M=V/V_g \ll 1$.

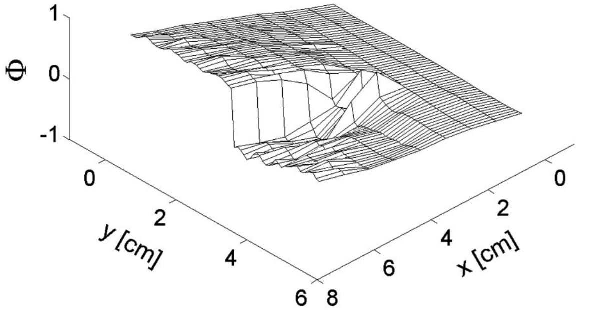

FIG. 14. Map of Φ in the xy plane close to the vortex core, the incident direction is x and fluid rotation is counterclockwise. $\lambda=1.2$ cm, $V_g=19$ cm/s, $\Gamma=20$ cm^2/s, and $b/\lambda \approx 0.8$.

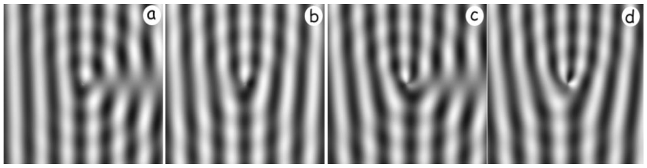

FIG. 15. Snapshots of dislocations resulting on electron wave function propagating from left to right, interacting with a counterrotating vector potential, calculated from Ref. [7]. (a) $b/\lambda=1/2$, (b) $b/\lambda=1$, (c) $b/\lambda=3/2$, and (d) $b/\lambda=2$.

We have measured the phase Φ of the dislocated wave with respect to the source (see Fig. 14), around the vortex, and observed thus the effect of the vorticity field on a plane fronted surface wave. As pointed out earlier, the slope of the phase as a function of x (incident direction) at a given position y is inversely proportional to the local wavelength. Then, Fig. 14 indicates that the velocity field introduces compression and dilation whose cumulative effect is responsible for dislocations in the wave front. As pointed out above, for low Mach numbers, the Burgers vector is predicted to increase linearly with Γ. In fact, for high values of Γ, the fluid speed near the vortex core is no longer small in comparison to the group velocity of the waves. For instance, for the case in Fig. 11 the Mach numbers close to the core (5 mm from the vortex center) are the following: (a) $M \approx 0.06$, (b) $M \approx 0.16$, (c) $M \approx 0.3$, and (d) $M \approx 0.47$. In a crude approximation, from relation (7), it can be deduced that the effect of the Mach number on the wave is to decrease the phase shift close to the vortex core. However, such a decrease is not observed within the resolution of our experiment. The experimental results in Fig. 13 satisfy the linear relation due to the advection effect; as we move away from the vortex, the Mach number decreases rapidly and no effect on the wave pattern is expected.

The appearance of topological dislocations is not specific to surface wave system. Indeed, our experiment possesses a close analogy with the Aharonov-Bohm effect. The simplest form of this effect, analogous to the surface wave-vortex interaction problem, occurs when a beam of particles of charge q and mass m is normally incident on a long thin cylinder containing a magnetic field $\vec{B}(x)$ (the analogous of the vorticity field) parallel to its axis. Outside the cylinder of finite radius (analogous of the vortex core) the vector potential $\vec{A}(x)$ (the velocity field) is an azimuthal vector whose absolute value decreases as $1/r$. Of course $\vec{B}=0$ outside the cylinder. Figure 15 shows patterns produced by the interaction of the electron wave function with filamentary magnetic field for increasing the magnetic flux Φ (the circulation Γ). These patterns, obtained numerically by using the Berry approach for the Aharonov-Bohm effect discussed in Ref. [10], should be contrasted to our experimental results presented in

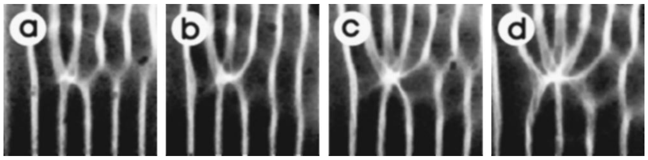

FIG. 16. Snapshots of experimental dislocations resulting on a surface wave propagating from left to right ($\lambda=1.4$ cm), interacting with a counterrotating vortex. (a) $b/\lambda=0.5$, (b) $b/\lambda=1.0$, (c) $b/\lambda=1.5$, and (d) $b/\lambda=2.0$.

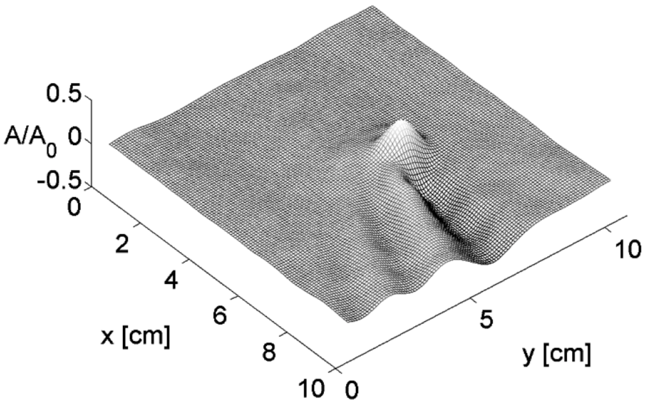

FIG. 17. Experimental surface deflection, obtained by scanning as described in the text, for $\Gamma \sim 6$ cm^2/s, $f = 18$ Hz, $\lambda = 1.1$ cm, and $V_g = 15.5$ cm/s.

Fig. 16. In the quantum case, the electron wave function has also a discontinuity corresponding to a dislocation whose Burgers vector obeys $b/\lambda = \Phi/hV_e\lambda$ [10]. Here V_e and λ are the group velocity and the wavelength of the electron wave function, respectively, and h is the Planck constant. This relation is the analog of Eq. (9) in which Γ is replaced by Φ/h.

C. Scattering cross section

In addition to the surface visualization described above, we have performed measurements of the amplitude of the surface wave by detecting the deflection of a laser beam reflected at the wavy water surface as explained in the experimental section. The accuracy of the measurements obtained via laser beam deflection is higher than image analysis, and it allows us to test the limits of theoretical approaches.

Figure 17 is an experimental spatial map of the wave amplitude for $\Gamma \sim 6$ cm^2/s, obtained by plotting at each point the maximum amplitude of the wave. Thus, this map does not contain phase information and the space variation in such amplitude corresponds to nodal and antinodal lines resulting from the interference between the incident and the scattered waves.

The information contained in Fig. 17 can be used to measure the scattering cross section of the surface wave by the vortex. Indeed, this is partially obtained by measuring the surface deflection following the angular direction for a given distance from the vortex core. Figure 18 is the ratio of the scattered wave amplitude A_s to the incident amplitude A_0 as a function of the polar angle θ for several values of b/λ and for a given frequency *f*. Here A_s is defined as $A_s = A - A_0$, where A is the total wave amplitude. Since oscillations in the measured amplitude A following the angular direction are due to constructive and destructive interferences between the incident and the scattered waves, the envelope of oscillations in A_s/A_0 is the scattering cross section which, as shown in Fig. 18, decreases with b/λ. The agreement with theoretical values reported in Ref. [12] is good for b/λ small and becomes poorer as b/λ increases; see Fig. 4 in Ref. [12]. We now compare the results obtained here with similar situations found in the Aharonov-Bohm effect. As reported in Ref. [12], mathematically both effects have the same structure giving rise to the same type of dislocations in the wave front. However, there are differences concerning the scattered wave; water waves penetrate inside the vortex, while electrons do not necessarily penetrate the solenoid. These differences do not affect the fact that in both cases there is a dislocated wave, but they do affect significantly the space distribution of the scattered wave. The most striking difference is that in the quantum mechanical case with impenetrable boundary conditions the scattered wave is symmetric. In the case of water waves, we have observed (see Fig. 17) that the scattered wave is asymmetric. This difference is due to the fact that water wave fronts are rotated by a finite amount inside the vortex. This rotation also occurs when electrons interact with a magnetic field. Indeed, as shown in Ref. [12] allowing the electron to penetrate inside the solenoid leads to an asymmetric scattered wave.

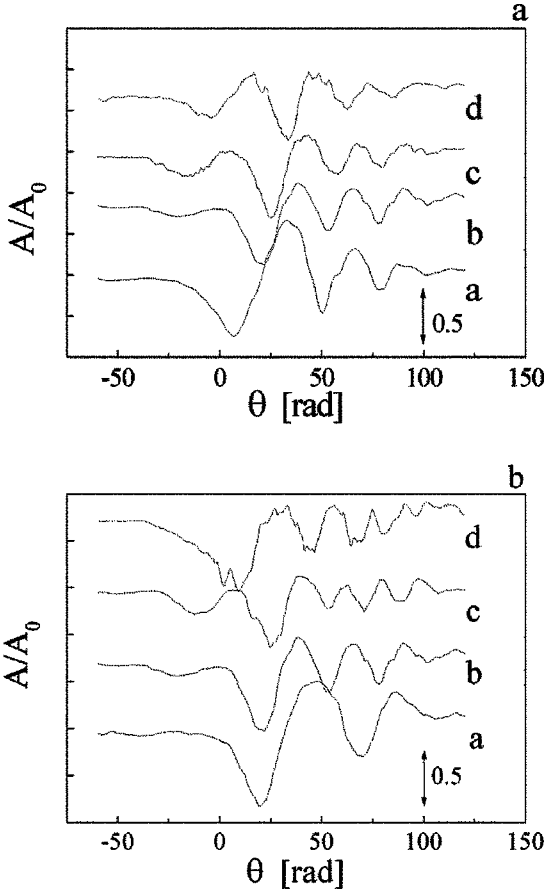

FIG. 18. Experimental amplitude of the surface wave A, normalized to the incident one A_0, obtained by scanning the water surface around the vortex following a circle of radius $r = 3$ cm. (a) For $f = 18$ Hz, $\lambda = 1.1$ cm, $V_g = 15.5$ cm/s, and several Burgers vectors b: Curve *a*: $b/\lambda \sim 0.5$; Curve *b*: $b/\lambda \sim 0.65$; Curve *c*: $b/\lambda \sim 0.8$; Curve *d*: $b/\lambda \sim 0.9$. (b) A/A_0 for constant $\Gamma \sim 16.5$ cm^2/s and several wavelength λ: Curve *a*: $\lambda = 2.25$ cm; Curve *b*: $\lambda = 1.4$ cm; Curve *c*: $\lambda = 1.1$ cm; *d*: $\lambda = 0.9$ cm.

Treatment reported in Ref. [12], being a leading order correction to the shallow water wave equation, considers wavelengths long compared to fluid depth, and does not in-

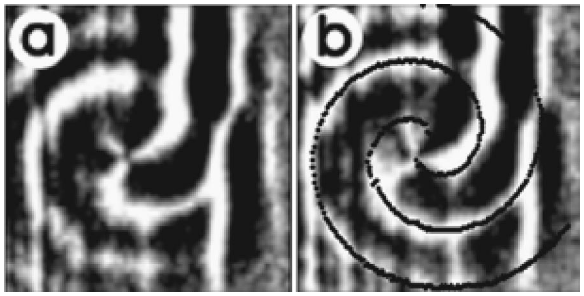

FIG. 19. Two snapshots, 1/30 s apart, of spiral scattered wave excited by a wave train that propagates from left to right of wavelength $\lambda = 1.2$ cm, $V_g = 22$ cm/s, at $\Gamma \approx 36$ cm^2/s. An emerging two-arm spiral is visible when the tail of the wave train (still visible on the right of the pictures) leaves the core region. The dotted line in (b) is the spiral shape calculated using the mathematical expression for the scattered wave deduced by Coste *et al.*

clude the possibility of the penetration length of the wave into the fluid being of the same order as the undisturbed surface deformation associated with the vortex. We believe that this fact may be at the root of the increasing disagreement between theory and experiment observed for increasing b/λ (see Fig. 4 in Ref. [12]). It is important to note that for the water surface wave case, both types of conditions can be obtained. For low values of Γ, the surface deflection at the vortex core is small and surface waves go inside the vortex. In contrast, for high values of Γ, surface deflection is larger and surface waves no longer penetrate the vortex core. However, the Burgers vector b/λ is a linear increasing function of circulation Γ in both cases.

D. Surface train wave interacting with the vortex

The scattered wave is relatively difficult to observe since it needs to be subtracted from the total wave. Instead of following such a procedure, we partially separate the wave emitted by the vortex from the incident one by using a short wave train as the excitation of the vortex. When the wave train leaves the vortex core, the scattered wave is visible for a few periods of oscillation. In the set of experiments presented here, the train wave of wavelength near 1 cm contains about three oscillations. With this method we have been able to observe isolated spirals for short periods as shown in Fig. 19. These spiral waves are visible preferentially when the surface deflection is large compared to the penetration depth of surface waves. Thus, spiral waves appear to be the natural solution for the scattering of planar surface waves by a vortex, in the case in which waves do not penetrate. We will see below that the number of arms of these kinds of spirals, for a given surface wave frequency, relates to vortex circulation.

E. Scattered spirals in the shallow water regime

For the purpose of this paper, it is illustrative to show that the existence of spiral solutions is predicted theoretically in the shallow water regime, see Fig. 20. For the sake of clarity, we have plotted separately the dislocated and scattered waves, calculated from the theoretical model proposed in Ref. [14], for impenetrable boundary conditions. We observe that when the dimensionless Burgers vector (b/λ) is an integer number, the scattered wave is always a spiral wave; see right panels in Fig. 20. In addition, if the Burgers vector is a multiple of half the wavelength, the scattered wave is spiral shaped but it contains a dislocation as shown in Fig. 21. It is interesting to look at the transition from a regular to dislocated spiral wave which always occurs for Burgers vector near a semi-integer value; see Fig. 22. It can be deduced from previous results that the number n of spiral arms links to the Burgers vector as $n \sim [b/\lambda + 1/2]$, where $[\cdots]$ indicates integer part. This result is nearly independent of the size of the impenetrable vortex core R. We have explored values of kR ranging from 0.2 to 4 observing only small changes on the scattered waves with no changes in its arms number. We have also found that similar spirals are present in the solution proposed by Berry *et al.* [10] for the Aharonov-Bohm problem, keeping the same characteristics as in the shallow water regime. In fact, as pointed out by Coste *et al.* [14], shallow water regime and Aharonov-Bohm case share the same kind of solutions.

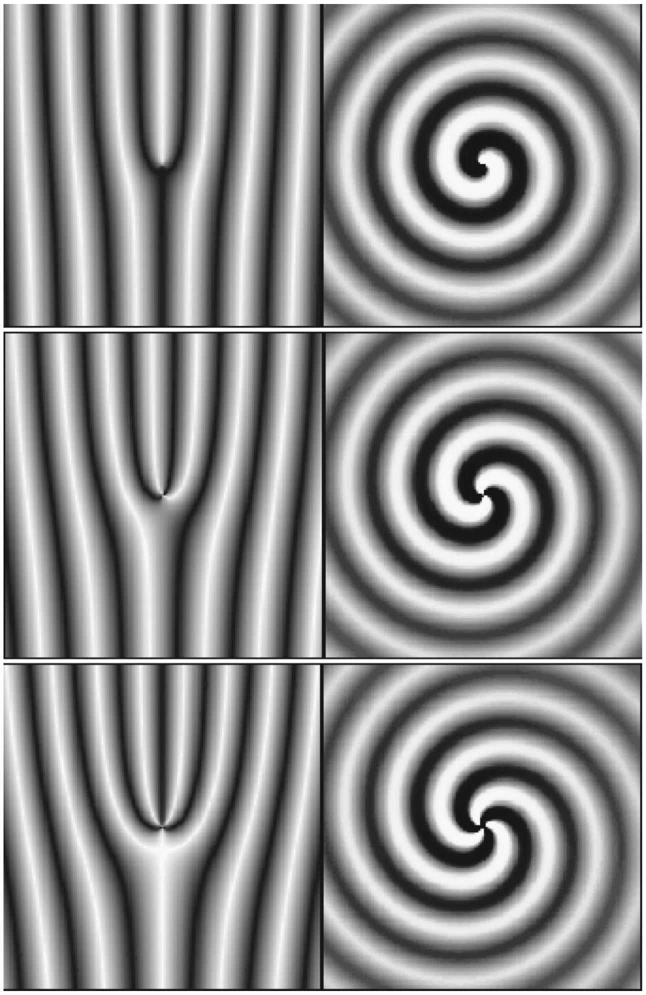

FIG. 20. Snapshots of dislocated (left) and scattered waves (right) obtained by calculating numerically the wave front solutions, proposed by Coste *et al.* for the shallow water regime, for $b/\lambda = 0,1,2$, and 3, respectively.

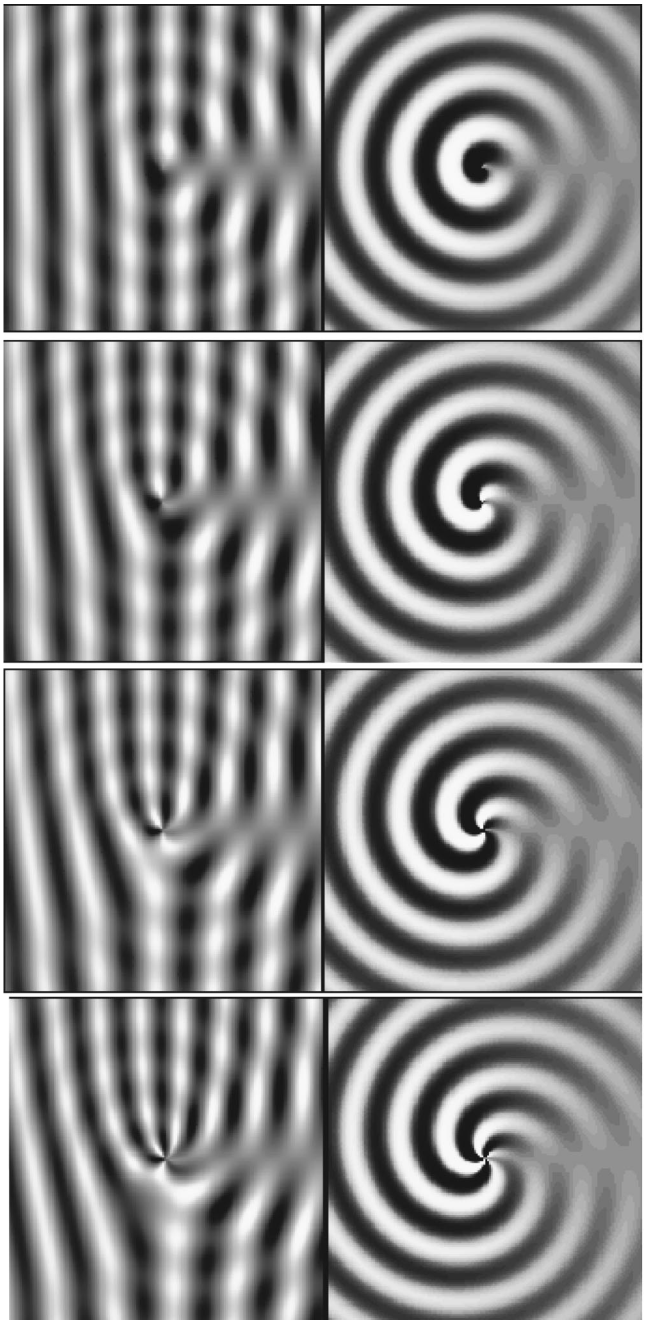

FIG. 21. Snapshots of dislocated and scattered waves calculated from Coste *et al.* for $b/\lambda=0.5,1.5,2.5,$ and 3.5, respectively.

To make contact with theoretical predictions presented above, we have measured the number of arms of spiral waves observed by the method described in Sec. V D. Figure 23 indicates this number as a function of the Burgers vector. Within the uncertainty of our experimental conditions, our results are consistent with those predicted in the preceding section. For $1/2<b/\lambda$ no spiral waves can be detected with our method; in the cases of $1/2<b/\lambda<3/2$ and $3/2<b/\lambda<5/2$ single-armed and two-arm spiral waves are observed, respectively.

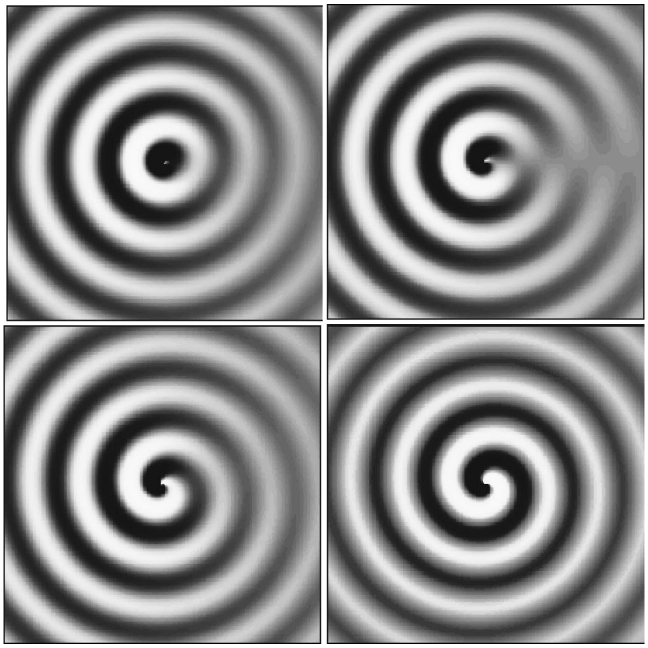

FIG. 22. Snapshots of scattered wave calculated from Coste *et al.* for $b/\lambda=0.4,0.5,0.6,$ and 1, respectively.

From a topological point of view, since the phase of the effective wave that impinges the vortex core has a topological defect, i.e., a dislocation, the existence of spiral waves seems natural in both the quantum and classical mechanical problems. Thus, spiral waves presented here are the solutions that respect boundary conditions at the impenetrable vortex core. These conditions predict that if the incident wave has a dislocation, the scattered one must present the same feature. In other words, a spiral wave can be seen as a dislocated circular wave. It is important to note that scattered spiral waves are neither predicted nor observed when the vortex core is penetrable. However, a theoretical prediction of the existence of spiral waves has been developed by Umeki and Lund [16] for the interaction of sound waves and a vortex core with penetrable boundary conditions for very low Mach

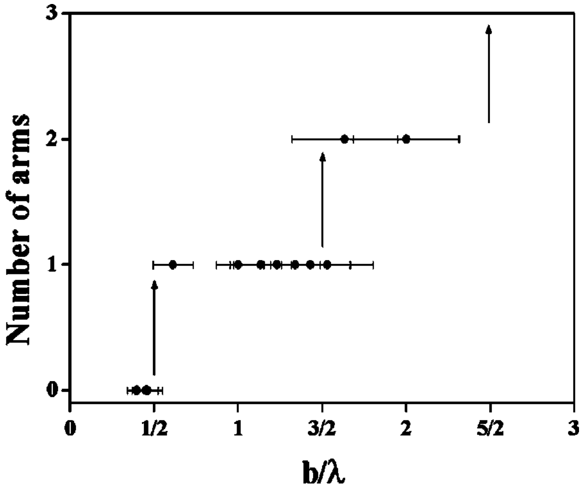

FIG. 23. Number of arms of spiral waves as a function of Burgers vector. Arrows show the locations of transitions of arm number, as predicted by both the shallow water and the Aharonov-Bohm cases.

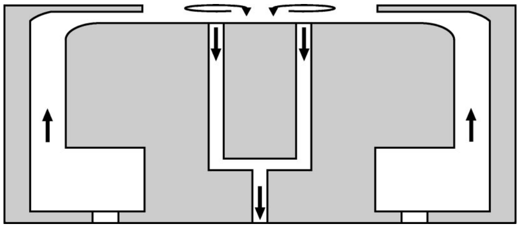

FIG. 24. Schema of the system to generate the two-vortex configuration.

number and very short wavelength compared to the radius of the vortex core. Using an asymptotic solution for $r \gg \lambda_s$ they have found that the number of spiral arms is given approximately by $\Gamma/V_{gs}\lambda_s \approx n/2$, which is twice the number of arms found in our experiment for the same circulation values. This discrepancy might be due to the fact that the calculated spiral waves are solutions at distances far from the vortex core, where the boundary conditions at the vortex core are no longer relevant. In contrast, in our case, spiral waves are the result of the symmetry breaking at the vortex core itself.

To conclude this section let us emphasize that a simple visualization of a plane wave interacting with a single vortex reveals dislocations in the wave front and the presence of a scattered wave. The effect of the vortex is twofold: the advection of the wave due to vortex circulation produces a phase shift responsible for dislocations and the vortex core is responsible for the scattered wave. We have checked that the Burgers vector in the regime accessible in our experiment is consistent with Berry's formula. However, the cross section does not follow Berry predictions [10], since in our case it is an asymmetric function of the azimuthal angle. As opposed to the case studied by Berry *et al.* [10], the surface wave penetrates inside the vortex core. Also, in our experiment, the group velocity is larger than, but it can become of the same order as, the maximum fluid velocity within the vortex core. Since the vortex core is responsible for the scattered wave, the question about the "supersonic" effect on the cross section due to high speed in the vortex core becomes a relevant issue.

VI. TWO-VORTEX-WAVE INTERACTION

We have seen in previous sections that the interaction of surface waves with a filamentary vortex is analogous to the simplest form of the Aharonov-Bohm effect. Such an analogy can be useful to illustrate some particular features of the physics of the vortex-electron interaction in quantum mechanics. For instance, this system can be a useful tool to study similar phenomena that usually appear in superconductors or superfluids [21]. As an example of the variety of experimental configurations that can be explored using surface waves, we investigate qualitatively the two-vortex-wave interaction problem.

In order to produce a stable vortex dipole, in our water tank apparatus, the two counterrotating vortices are generated by extracting the water throughout two holes, 4 mm in diameter and located a distance $d = 2$ cm apart, see Fig. 24.

The outcoming fluid is reinjected homogeneously in the radial direction through a ring-shaped gap, 6 cm in diameter. Thus, the incoming radial flow does not add any vertical vorticity to the system. One way to control the vortex rotation sense is by slightly breaking the symmetry of the radial flow along an axis parallel to the one that contains the vortex dipole. In Figs. 25(a) and 25(b), the vortex dipole is perpendicular to the incident wave vector; we notice that similar to what occurs in the case of one vortex, the wave front exhibits a phase shift that is proportional to Γ. However, here the dipole does not break the symmetry of the wave front. The whole wave front is advanced, Fig. 25(a), or retarded, Fig. 25(b), over a distance defined by the vortex separation d. When the dipole is parallel to $\vec{k}$, as in Fig. 25(c), the situation is rather different, the phase shift induced by the first vortex is compensated by the second vortex in such a way that no net effect is observed in the wave front far from the vortex. The general case illustrated in Fig. 25(d) shows that the effect of the dipole on the wave front is over a distance that corresponds to the absolute value of $d \sin(\vec{k},\vec{d})$, where $\vec{d}$ goes from the negative to the positive vortex. Thus, the size of the dislocation "loop" introduced on the wave front by the vortex dipole vanishes when the dipole is parallel or antiparallel to $\vec{k}$. When the vortex dipole is perpendicular to incident direction, we have followed small particle trajectories to measure the circulation at a distance 0.8 mm from one of the vortices. For circulation values, calculated with this procedure smaller than $\Gamma < 6$ cm^2/s, we found that the phase shift induced by the dipole is roughly a linear function of Γ, as in Eq. (9). However, when circulation is increased, this

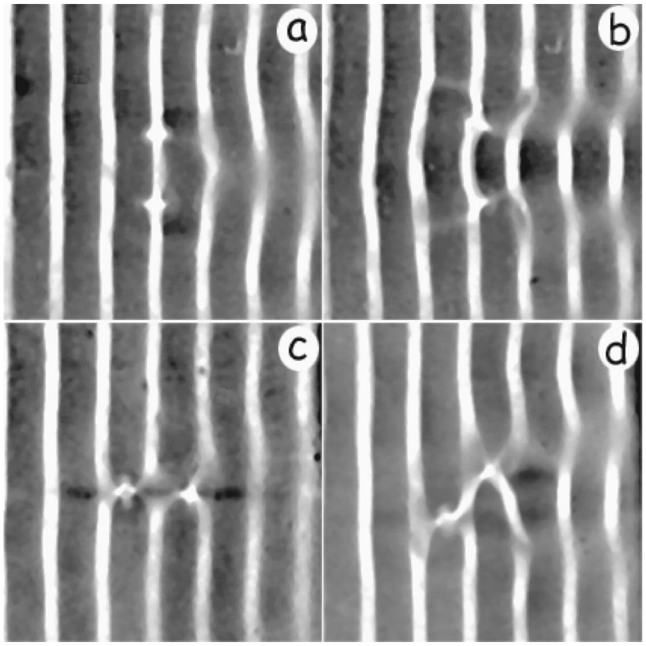

FIG. 25. Snapshots of wave pattern for several orientations of the vortex dipole. In all panels, the wave propagates from left to right. The wave vector $\vec{k}$, contained in the figure plane, is then positive. In (a) and (b) the dipole axis, also contained in the figure plane, is perpendicular to the wave vector. In (a) the dipole is positive and negative in (b). In (c) the dipole is antiparallel to $\vec{k}$. In (d) it makes an angle of about $-3\pi/4$ with $\vec{k}$.

relation is no longer valid and the interaction between the two vortices becomes a relevant issue.

VII. CONCLUDING REMARKS

In conclusion, we have found that simple visualization of a surface plane wave interacting with a single vortex reveals dislocations in the wave front and the presence of a scattered wave. The effect of the vortex is twofold: the advection of the wave due to vortex circulation produces a phase shift responsible for dislocations, the vortex core in turn is responsible for the scattered wave. We have checked that the Burgers vector in the regime accessible to our experiment is consistent with our simple analysis and the quantum mechanics analog introduced by Berry.

On the other hand, for low values of Γ the scattering cross section resulted an asymmetric function with respect to an axis containing the vortex core and parallel to the incident wave vector. This result contrasts with calculations [10] for the quantum mechanics case. The difference arises as a consequence of the rigid character of the solenoid. In fact, as opposed to the case studied by Berry, the surface wave penetrates the vortex core; the wave is then deflected by the core similarly to what occurs for a light ray when it crosses a region of varying refraction index. In the case of quantum mechanics when the electrons are mathematically allowed to move inside the solenoid, the scattered wave function has the same features as surface waves in the low Γ regime. Our investigations exploring configurations with more than one vortex support the interpretation of dislocations as dilation and compression induced by the flow gradient in the wave front. Two counterrotating vortices have only a local effect on the wave front when the dipole coincides with propagation direction. When the dipole is perpendicular to the wave vector a symmetric phase shift is induced in the wave front and the effect is the superposition of each vortex separately. The general case is more complicated, however our results suggest the absolute value of $d\sin(\vec{k},\vec{d})$ accounts for the range of the wave front distortion.

Finally, let us emphasize that more complex vorticity configurations can be explored and learned to make contact with quantum mechanics problems, usually not accessible experimentally.

ACKNOWLEDGMENTS

It is a pleasure to thank F. Lund, E. Hann, P. Coullet, and J.-C. Géminard for many enlightening discussions. This work was supported by a ‘‘Cátedra Presidencial en Ciencias’’ and Conicyt, under Fondap Project No. 11980002.

---

[1] U. Frisch, *Turbulence* (Cambridge University Press, Cambridge, 1995), Chap. 8.

[2] C. Baudet, S. Ciliberto, and J.F. Pinton, Phys. Rev. Lett. **67**, 193 (1991).

[3] P. Roux and M. Fink, Europhys. Lett. **32**, 25 (1995); M. Fink, Phys. Today **50**(3), 34 (1997). .

[4] P. Roux, J. de Rosny, M. Tanter, and M. Fink, Phys. Rev. Lett. **79**, 3170 (1997).

[5] S. Manneville, JH. Robres, A. Maurel, P. Petitjeans, and Phys. Fluids **11**, 3380 (1999).

[6] S. Manneville, P. Roux, M. Tanter, A. Maurel, M. Fink, F. Bottausci, and P. Petitjeans, Phys. Rev. E **63**, 036607 (2001).

[7] R. Labbé and J.F. Pinton, Phys. Rev. Lett. **81**, 1413 (1998).

[8] J-H. Shyo and O.M. Phillips, J. Fluid Mech. **217**, 115 (1990).

[9] M.S. Longuet-Higgins, J. Fluid Mech. **308**, 15 (1996).

[10] M.V. Berry, R.G. Chambers, M.D. Large, C. Upstill, and J.C. Walmsley, Eur. J. Phys. **1**, 154 (1980).

[11] Y. Aharonov and D. Bohm, Phys. Rev. Lett. **115**, 485 (1959); for reviews see I. Olariu and I.I. Popescu, Rev. Mod. Phys. **57**, 339 (1985); M. Peshkin and A. Tonomura, *The Aharonov-Bohm Effect*, Lectures Notes in Physics Vol. 340 (Springer, Berlin, 1989).

[12] F. Vivanco, F. Melo, Ch. Coste, and F. Lund, Phys. Rev. Lett. **83**, 1966 (1999).

[13] F. Vivanco and F. Melo, Phys. Rev. Lett. **85**, 2116 (2000).

[14] The relation between the Aharonov-Bohm effect and the scattering of surface wave by a vortex was studied, in the limit of wavelengths short compared to vortex core radius by C. Coste, F. Lund, and M. Umeki, Phys. Rev. E **60**, 4908 (1999); C. Coste, and F. Lund, *ibid.* **60**, 4917 (1999).

[15] F. Lund and C. Rojas, Physica D **37**, 508 (1989).

[16] M. Umeki and F. Lund, Fluid Dyn. **21**, 201 (1997).

[17] This relation is only valid outside the vortex core since it is derived by assuming that the flow is irrotational.

[18] S. Douady, J. Fluid Mech. **221**, 383 (1990).

[19] Landau Lifchitz, *Mécanique des Fluides* (MIR, Moscow, 1971), p. 124.

[20] See, for instance, J.-F. Joanny, Thèse de Doctorat d‘Etat, Université Pierre et Marie Curie Paris 6, 1985.

[21] The phonon-vortex interaction in superfluids has been the subject of recent debate: see C. Wexler *et al.*, Phys. Rev. Lett. **81**, 4277 (1998); E.B. Sonin, *ibid.* **81**, 4276 (1998), and references therein.